# Integrating the Normal Field of a Surface in the Presence of Discontinuities

Jean-Denis Durou[1,2], Jean-François Aujol[1], and Frédéric Courteille[3]

[1] CMLA, ENS Cachan, CNRS, Universud, Cachan, France
[2] IRIT, Université Paul Sabatier, Toulouse, France
[3] LGC, Université Paul Sabatier, Toulouse, France

**Abstract.** We show how to integrate the normal field of a surface in the presence of discontinuities by three different ways. We obtain very satisfactory 3D-reconstructions, from the point of view of the accuracy of the reconstructions. As an important consequence, no prior segmentation of the scene into parts without discontinuity is required anymore. Finally, we test the three proposed methods of integration in the framework of photometric stereo, a technique which aims at computing the normal field of a scene surface from several images of this scene lighted under different directions.

## 1 Introduction

Computing the 3D-shape of a surface from a collection of normals is not so straightforward as it could appear, even in the case of a dense normal field i.e., when the normal to the surface is known at each pixel of an image. This classical problem of 3D-reconstruction, which is usually called normal field integration, has been solved using either the calculus of variations [1], direct integration [2] or frequency-domain methods [3,4]. In a previous work [5], we improved the original algorithm by Horn and Brooks [1] in two ways: we showed that the knowledge of the height on the boundary, a knowledge which is usually not available, is not required; we also showed how to take perspective into account. In the present paper, we propose a novel improvement of this algorithm which is compatible with the previous ones: we show how to deal with discontinuous surfaces, a situation which occurs in practice as soon as there are occlusions. This improvement allows us to integrate the normal field on a whole dense normal field, without need for prior segmentation into several parts without discontinuity.

In Section 2, we recall the basic equations of normal integration. In Section 3, Horn and Brooks' algorithm and our previous improvements are presented. In Section 4, three new methods of integration of a normal field are exhibited, compared and tested on a normal field computed by photometric stereo from real images. Section 5 summarizes the main contributions of the paper.

## 2 Basic Equations of Normal Integration

Suppose that, in each point $Q = (x, y)$ in the image of a surface $\mathcal{S}$, we know the unit outgoing normal $\mathbf{n}(x, y) = [n_X(x, y), n_Y(x, y), n_Z(x, y)]^t$. Then, the function

D. Cremers et al. (Eds.): EMMCVPR 2009, LNCS 5681, pp. 261–273, 2009.

$\mathbf{n}$ is a dense normal field. Integrating a normal field $\mathbf{n}$ consists in searching for the shape $\mathcal{S}$ i.e., for three functions $X$, $Y$ and $Z$ such that the normal to $\mathcal{S}$ at the point $P = [X(x,y), Y(x,y), Z(x,y)]^t$ conjugated with $Q$ is $\mathbf{n}(x,y)$. Due to the lack of space, no rigorous state-of-the-art on the integration of a normal field is done (see e.g. [6,7,8]). Let us also cite [9], in which the problem of integrating a sparse normal field is addressed.

Let us first recall the fundamental equations of normal integration. For the sake of simplicity, we will omit the dependences in $(x,y)$. Either for orthographic or for perspective projection, it is easy to show that $X$ and $Y$ can be deduced from $Z$. Under the assumption of orthographic projection, the depth $Z$ can be computed thanks to the following elementary PDE:

$$\nabla Z = \frac{1}{g}\,[p,q]^t, \tag{1}$$

where $p = -n_X/n_Z$ and $q = -n_Y/n_Z$, and $g$ denotes the image magnification. Thus, the problem of integrating a normal field is that of integrating the gradient of $Z$. It has been shown in [5] that a strict analogy exists between the perspective case and the orthographic case, provided that a change in the unknown is done:

$$\mathcal{Z} = \ln|Z|. \tag{2}$$

The new unknown $\mathcal{Z}$ satisfies the following PDE, which is similar to (1):

$$\nabla \mathcal{Z} = [r,s]^t, \tag{3}$$

with the following definitions of $r$ and $s$:

$$\begin{aligned} r &= -\frac{n_X}{x\,n_X + y\,n_Y + f\,n_Z}, \\ s &= -\frac{n_Y}{x\,n_X + y\,n_Y + f\,n_Z}, \end{aligned} \tag{4}$$

where $f$ denotes the focal length of the camera. Here again, the problem of integrating a normal field is that of integrating the gradient of $\mathcal{Z}$.

In order to ensure that the normal field is integrable i.e., that Eqs. (1) or (3) can be integrated whatever the integration path, it is necessary and sufficient that $p$ and $q$ (in the orthographic case) or $r$ and $s$ (in the perspective case) satisfy the Schwartz equations $\partial p/\partial y = \partial q/\partial x$ or $\partial r/\partial y = \partial s/\partial x$. In practice, a normal field is never rigorously integrable. There are two classical ways of dealing with this problem. The first one consists in using several integration paths, and then to mean the different integrals [2]. The second solution consists in considering Eqs. (1) or (3) as optimization problems [1]. Apart from their slowness, these last methods of integration have two main advantages: on the one hand, they are more robust to noise; on the other hand, in the case where the Schwartz equation is not satisfied, they provide however an acceptable shape. In the following of the paper, we will focus on this second solution. It is noteworthy that considering the orthographic case is enough, since Eqs. (1) and (3) are similar. The only difference is that Eq. (3) requires the knowledge of the focal distance $f$, as well

as the location of the principal point, because these parameters occur in the definitions (4) of $r$ and $s$: explicitly for $f$; implicitly for the location of the principal point, since the coordinates $x$ and $y$ of a pixel depend on it.

## 3 Integration Using Quadratic Regularization

### 3.1 Continuous Formulation

For the sake of simplicity, let us suppose that $g = 1$. The resolution of Eq. (1) using quadratic regularization amounts to minimizing the following functional:

$$\mathcal{Q}(Z) = \iint_{(x,y)\in\Omega} \|\nabla Z(x,y) - \mathbf{v}(x,y)\|^2 \, dx \, dy, \tag{5}$$

where $\Omega$ is the "domain of reconstruction", $\nabla Z = [Z_x, Z_y]^t$ stands for the gradient of $Z$, and $\mathbf{v} = [p, q]^t$ is the "reduced normal field" i.e., the datum. Quadratic regularization is known to work well in the case of smooth surfaces. A straightforward computation gives:

$$\nabla\mathcal{Q}(Z) = -2\,\mathrm{div}\,(\nabla Z - \mathbf{v}). \tag{6}$$

It follows that the Euler-Lagrange equation associated to $\mathcal{Q}(Z)$ is:

$$\mathrm{div}\,\nabla Z = \mathrm{div}\,\mathbf{v}. \tag{7}$$

This is a Poisson equation, which is easy to solve, even analytically [10]. Nevertheless, solving Eq. (7) is equivalent to searching for an extremum of $\mathcal{Q}(Z)$ only if $Z$ is constrained on the boundary $\partial\Omega$ of $\Omega$. Otherwise, this equation has to be complemented with the "natural boundary equation" at each point of the boundary $\partial\Omega$, which is here the Neumann boundary condition $(\nabla Z - \mathbf{v})\cdot\mathbf{N} = 0$, where the vector $\mathbf{N}$ is normal to $\partial\Omega$ in the image plane.

### 3.2 Improved Horn and Brooks' Scheme

Horn and Brooks propose in [1] a resolution of Eq. (7) that comes from the following approximation of the expression (5) of $\mathcal{Q}(Z)$:

$$\mathcal{E}(\mathbf{Z}) = \sum_{(i,j)\in\Omega'}\sum \left[\frac{Z_{i+1,j} - Z_{i,j}}{\delta} - \frac{p_{i+1,j} + p_{i,j}}{2}\right]^2 + \left[\frac{Z_{i,j+1} - Z_{i,j}}{\delta} - \frac{q_{i,j+1} + q_{i,j}}{2}\right]^2. \tag{8}$$

In this expression, $\delta$ denotes the distance between neighbouring pixels, $\Omega'$ the set of pixels $(i,j) \in \Omega$ such that $(i+1,j) \in \Omega$ and $(i,j+1) \in \Omega$, and $\mathbf{Z}$ the vector $[Z_{i,j}]_{(i,j)\in\mathring{\Omega}}$, where $\mathring{\Omega} = \Omega\backslash\partial\Omega$ is the set of pixels $(i,j) \in \Omega$ whose four nearest neighbours are in $\Omega$. The values $Z_{i,j}$ of the pixels lying on $\partial\Omega$ are not considered as unknowns, since Horn and Brooks use a Dirichlet boundary condition. For

the sake of simplicity, let us suppose that $\delta = 1$. For a pixel $(i,j) \in \mathring{\Omega}$, one gets from the characterization $\nabla\mathcal{E} = 0$ of an extremum and from (8):

$$4\,Z_{i,j} - (Z_{i+1,j} + Z_{i,j+1} + Z_{i-1,j} + Z_{i,j-1}) + \frac{p_{i+1,j} - p_{i-1,j} + q_{i,j+1} - q_{i,j-1}}{2} = 0. \tag{9}$$

This equation is a discrete approximation of Eq. (7). Horn and Brooks solve Eq. (9) using the following iteration [1]:

$$Z_{i,j}^{k+1} = \frac{Z_{i+1,j}^k + Z_{i,j+1}^k + Z_{i-1,j}^k + Z_{i,j-1}^k}{4} - \frac{p_{i+1,j} - p_{i-1,j} + q_{i,j+1} - q_{i,j-1}}{8}. \tag{10}$$

The initialization is not a cause for concern, since the functional $\mathcal{Q}(Z)$ is convex. In our experiments, we use $Z^0 = 0$.

In order to avoid the need for $Z$ on the boundary, it suffices to consider that all the values $Z_{i,j}$, for $(i,j) \in \Omega$, are unknowns. This implies that the equations $\partial\mathcal{E}/\partial Z_{i,j} = 0$, for $(i,j) \in \partial\Omega$, are not written under the form (9). For example, if $(i,j) \in \Omega' \cap \partial\Omega$, then (10) has to be replaced with:

$$Z_{i,j}^{k+1} = \frac{Z_{i+1,j}^k + Z_{i,j+1}^k}{2} - \frac{p_{i+1,j} + p_{i,j} + q_{i,j+1} + q_{i,j}}{4}. \tag{11}$$

In fact, equations such as (11) are nothing else than a discrete version of the natural boundary condition. This improvement of Horn and Brooks' scheme [5] is denoted $IS_{L_2}$.

### 3.3 Limits of the Improved Horn and Brooks' Scheme

Some of the computer vision techniques for 3D-reconstruction, as shape-from-shading, photometric stereo or shape-from-texture, first compute a normal field, and then need to integrate this normal field. Among them, photometric stereo is particularly interesting, since the computation of the normals is well-posed as soon as at least three images, taken using the same camera pose but different lightings, are available. Therefore, photometric stereo, a technique which has known a renewal in the last years [8,11,12], is well indicated to evaluate the methods of integration.

In [5], $IS_{L_2}$ was tested on three photographs of a Beethoven's bustle (see Fig. 1-left) which are available on the web[1]. Moreover, estimates of the three lightings are provided as well. The computed shape is qualitatively very good (see Fig. 1-right). Nevertheless, the goal of this paper is to propose some improvements for scheme $IS_{L_2}$. In fact, it is well-known that quadratic regularization is not well adapted to discontinuities. Let us now test $IS_{L_2}$ on the reduced normal field $\mathbf{v}_b$ of the benchmark surface $\mathcal{S}_b$ shown in Fig.2-left. The 3D-reconstruction which is obtained after $100 \times 128$ iterations of $IS_{L_2}$ is qualitatively very bad (see Fig. 2-right). Nevertheless, we will see further the usefulness of this final

[1] http://www.ece.ncsu.edu/imaging/Archives/ImageDataBase/Industrial/

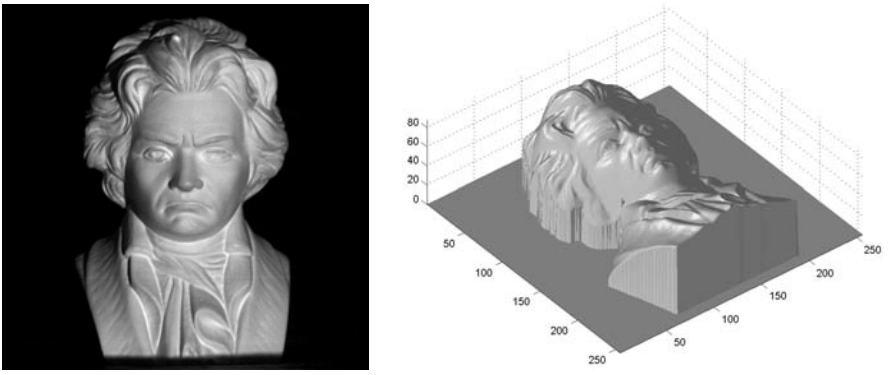


**Fig. 1.** Left: one of the three photographs of a Beethoven's bustle lighted under different directions. Right: 3D-reconstruction obtained from these three photographs using photometric stereo at each pixel on the bustle, then integrating the computed normal field using $IS_{L_2}$ (the depth $Z$ of the background is arbitrarily put to 0).

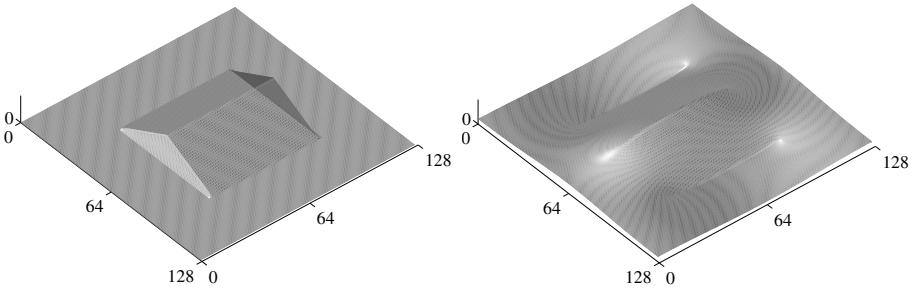


**Fig. 2.** Left: benchmark surface $\mathcal{S}_b$ with discontinuous depth $Z_b$ and discontinuous reduced normal field $\mathbf{v}_b$.Right: 3D-reconstruction obtained using $IS_{L_2}$: $\|\Delta Z\|_2 = 2.48$. The integration is performed on the whole domain $[1, 128]\times[1, 128]$. This depth function is denoted $Z_{L_2}$.

configuration $Z_{L_2}$. More precisely, let us introduce, as a quantitative evaluation of the reconstructions, the minimal root mean square error $\|\Delta Z\|_2$ between a 3D-reconstruction and the ground truth i.e., the root mean square error which corresponds to their best matching. Between $Z_{L_2}$ and the ground truth $Z_b$ of $\mathcal{S}_b$, we find $\|\Delta Z\|_2 = 2.48$. In the following of the paper, the use of other regularizers will allow us to reach much lower values for $\|\Delta Z\|_2$.

## 4 Integration Using Non-quadratic Regularization

### 4.1 Introduction

By analogy with regularization methods in image processing, it is tempting to consider other regularization choices. In image restoration, quadratic regularization

is indeed famous for its ease of use, but notorious for its lack of ability to recover sharp edges. It has been proposed to use regularization functions $\phi$ which both smooth the data in homogeneous regions but keep sharp edges by avoiding smoothing in non-homogeneous regions (see e.g. [13] and references therein for a detailed review of such methods in image restoration).

Let us now consider the following functional:

$$\mathcal{F}_\phi(Z) = \iint\limits_{(x,y)\in\Omega} \phi(\|\nabla Z(x,y) - \mathbf{v}(x,y)\|)\, dx\, dy. \tag{12}$$

Of course, this general form includes the quadratic regularization case (5) when $\phi(s) = s^2$.

A straightforward computation gives, from (12):

$$\nabla\mathcal{F}_\phi(Z) = -\mathrm{div}\left(\frac{\phi'(\|\nabla Z - \mathbf{v}\|)}{\|\nabla Z - \mathbf{v}\|}(\nabla Z - \mathbf{v})\right). \tag{13}$$

The optimality condition (Euler-Lagrange equation) $\nabla\mathcal{F}_\phi(Z) = 0$ can then be used to compute a numerical solution, as explained in the following subsections.

### 4.2 Linear Growth Regularization

For the sake of clarity, we detail here a first example of non-quadratic regularization. Let us consider the case of a linear growth functional [14], that is let us choose $\phi(s) = \sqrt{s^2 + \alpha^2}$ in functional (12) which then reads:

$$\mathcal{L}(Z) = \iint\limits_{(x,y)\in\Omega} \sqrt{\|\nabla Z(x,y) - \mathbf{v}(x,y)\|^2 + \alpha^2}\, dx\, dy. \tag{14}$$

Ideally, we would choose $\alpha = 0$. For image restoration, $\alpha = 1$ is a good choice when the greylevel values are in $[0, 255]$. The gradient (13) of the functional in this particular case becomes:

$$\nabla\mathcal{L}(Z) = -\mathrm{div}\left(\frac{\nabla Z - \mathbf{v}}{\sqrt{\|\nabla Z - \mathbf{v}\|^2 + \alpha^2}}\right). \tag{15}$$

Therefore, the Euler-Lagrange equation associated with the functional $\mathcal{L}(Z)$ is:

$$\mathrm{div}\left(\frac{\nabla Z}{\sqrt{\|\nabla Z - \mathbf{v}\|^2 + \alpha^2}}\right) = \mathrm{div}\left(\frac{\mathbf{v}}{\sqrt{\|\nabla Z - \mathbf{v}\|^2 + \alpha^2}}\right), \tag{16}$$

with Neumann boundary condition on $\partial\Omega$. Eq. (16) is much less tractable than Eq. (7). A way of computing its solution consists in using a semi-implicit scheme: we implicit the linear part of the equation, but its non-linear parts remain explicit. This gives:

$$\mathrm{div}\left(\frac{\nabla Z^{k+1}}{\sqrt{\|\nabla Z^k - \mathbf{v}\|^2 + \alpha^2}}\right) = \mathrm{div}\left(\frac{\mathbf{v}}{\sqrt{\|\nabla Z^k - \mathbf{v}\|^2 + \alpha^2}}\right). \tag{17}$$

Our first new scheme of integration, denoted $IS_{L_1}$, is as follows for $(i,j) \in \mathring{\Omega}$:

$$Z_{i,j}^{k+1} = \frac{1}{2d_{i,j}^k + d_{i-1,j}^k + d_{i,j-1}^k}[d_{i,j}^k(Z_{i+1,j}^k + Z_{i,j+1}^k) + d_{i-1,j}^k Z_{i-1,j}^k + d_{i,j-1}^k Z_{i,j-1}^k - d_{i,j}^k \frac{p_{i,j} + p_{i+1,j} + q_{i,j} + q_{i,j+1}}{2} + d_{i-1,j}^k \frac{p_{i,j} + p_{i-1,j}}{2} + d_{i,j-1}^k \frac{q_{i,j} + q_{i,j-1}}{2}], \tag{18}$$

where the factors $d_{i,j}^k$ denote the following discrete approximations of the denominators of Eq. (17):

$$d_{i,j}^k = \frac{1}{\sqrt{(Z_{i+1,j}^k - Z_{i,j}^k - \frac{p_{i,j} + p_{i+1,j}}{2})^2 + (Z_{i,j+1}^k - Z_{i,j}^k - \frac{q_{i,j} + p_{i,j+1}}{2})^2 + \alpha^2}}. \tag{19}$$

For the same reasons as in the case of quadratic regularization, $Z^0 = 0$ is used as initial configuration, and Eq. (18) has to be modified for pixels $(i,j)$ lying on the boundary $\partial\Omega$.

### 4.3 Non-convex Regularization

Let us now consider functional (12) in general. In image restoration [13], the regularization functions $\phi$ are usually called "$\phi$-functions". Such functions are required to have a linear growth around zero (to preserve edges), and a sublinear growth at infinity (so that high values of the argument are not penalized too much). We will consider both following classical $\phi$-functions:

$$\begin{aligned} \phi_1(s) = \ln(s^2 + \beta^2) \quad &\Rightarrow \quad \phi_1'(s) = \frac{2s}{s^2 + \beta^2}, \\ \phi_2(s) = \frac{s^2}{s^2 + \gamma^2} \quad &\Rightarrow \quad \phi_2'(s) = \frac{2\gamma^2 s}{(s^2 + \gamma^2)^2}. \end{aligned} \tag{20}$$

We a priori prefer this last choice, since $\phi_2(s)$ remains less than 1 when $s$ tends towards $+\infty$. Moreover, with this last choice:

$$\phi_2(s) = \frac{(s/\gamma)^2}{1 + (s/\gamma)^2}. \tag{21}$$

This means that the parameter $\gamma$ controls the large values of $s$. In the case of noisy data, we will use a greater value for $\gamma$ than in the case of non-noisy data.

Notice that with the choices of either $\phi_1$ or $\phi_2$, functional (12) is no longer convex (contrary to both functionals (5) and (14)). There may then be several minimizers. In our numerical experiments, we will have to face this problem.

The Euler-Lagrange equations associated to the functionals $\mathcal{F}_{\phi_1}(Z)$ and $\mathcal{F}_{\phi_2}(Z)$ are, respectively:

$$\begin{aligned} \text{div}\left[\frac{\nabla Z}{\|\nabla Z - \mathbf{v}\|^2 + \beta^2}\right] &= \text{div}\left[\frac{\mathbf{v}}{\|\nabla Z - \mathbf{v}\|^2 + \beta^2}\right], \\ \text{div}\left[\frac{\nabla Z}{(\|\nabla Z - \mathbf{v}\|^2 + \gamma^2)^2}\right] &= \text{div}\left[\frac{\mathbf{v}}{(\|\nabla Z - \mathbf{v}\|^2 + \gamma^2)^2}\right], \end{aligned} \tag{22}$$

with Neumann boundary conditions on $\partial\Omega$. There are strong similarities between both these equations and Eq. (16). The numerical schemes that we use to solve them are the same as (18), except that the factors $d_{i,j}^k$ must be replaced, respectively, with $e_{i,j}^k$ and $f_{i,j}^k$:

$$\begin{aligned} e_{i,j}^k &= \frac{1}{(Z_{i+1,j}^k - Z_{i,j}^k - \frac{p_{i,j}+p_{i+1,j}}{2})^2 + (Z_{i,j+1}^k - Z_{i,j}^k - \frac{q_{i,j}+p_{i,j+1}}{2})^2 + \beta^2}, \\ f_{i,j}^k &= \frac{1}{\left[(Z_{i+1,j}^k - Z_{i,j}^k - \frac{p_{i,j}+p_{i+1,j}}{2})^2 + (Z_{i,j+1}^k - Z_{i,j}^k - \frac{q_{i,j}+p_{i,j+1}}{2})^2 + \gamma^2\right]^2}. \end{aligned} \tag{23}$$

These schemes will be denoted, respectively, by $IS_{\phi_1}$ and $IS_{\phi_2}$.

### 4.4 Numerical Evaluation of the New Algorithms

In this subsection, we are going to test the three new schemes $IS_{L_1}$, $IS_{\phi_1}$ and $IS_{\phi_2}$ on the reduced normal field $\mathbf{v}_b$ of the benchmark surface $\mathcal{S}_b$ (see Fig. 2-left). As each of these schemes depends on one parameter, respectively $\alpha$, $\beta$ and $\gamma$, we must first study the influence of this parameter on the accuracy of the reconstruction.

The accuracy $\|\Delta Z\|_2$ of the 3D-reconstruction obtained using the scheme $IS_{L_1}$, in function of $\alpha$, is plotted on the left of Fig. 3. The best reconstruction, which is represented in Fig. 4, corresponds to $\|\Delta Z\|_2 = 1.66$ and is reached when $\alpha = 0.055$. It looks indeed a little more similar to $\mathcal{S}_b$ than the surface represented in Fig. 2-right, with a lower value of $\|\Delta Z\|_2$. However, this result is not fully satisfactory. The evolution of $\|\Delta Z\|_2$ in function of the number of iterations, which is represented on the right of Fig. 3, shows the convergent behaviour of $IS_{L_1}$ (we proved that $IS_{L_1}$ is a convergent scheme, but due to lack of space, the proof is not included in the paper; see [15] for further details). This curve also tells us that a fixed number of $100 \times 128$ iterations gives a good approximation

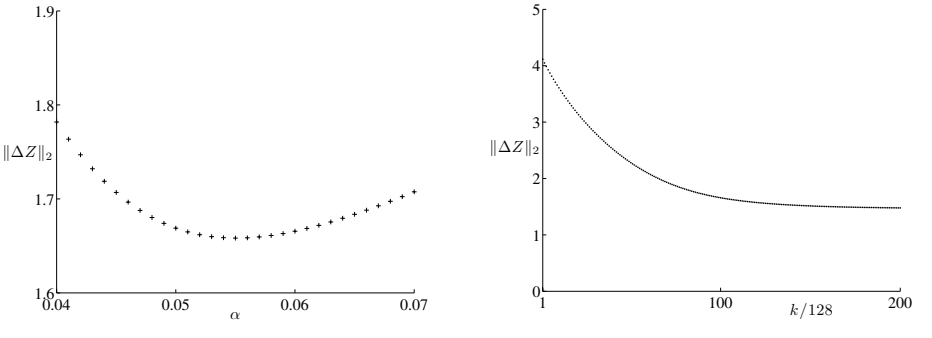


**Fig. 3.** Left: $\|\Delta Z\|_2$ in function of $\alpha$, after $100 \times 128$ iterations of $IS_{L_1}$. Right: $\|\Delta Z\|_2$ in function of the number of iterations of $IS_{L_1}$, for the optimal value $\alpha^* = 0.055$. In these tests, the initialization $Z^0 = 0$ is used.

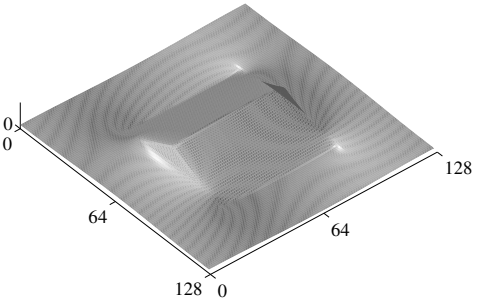


**Fig. 4.** 3D-reconstruction obtained using $IS_{L_1}$, for the optimal value $\alpha^* = 0.055$ and $Z^0 = 0$: $\|\Delta Z\|_2 = 1.66$

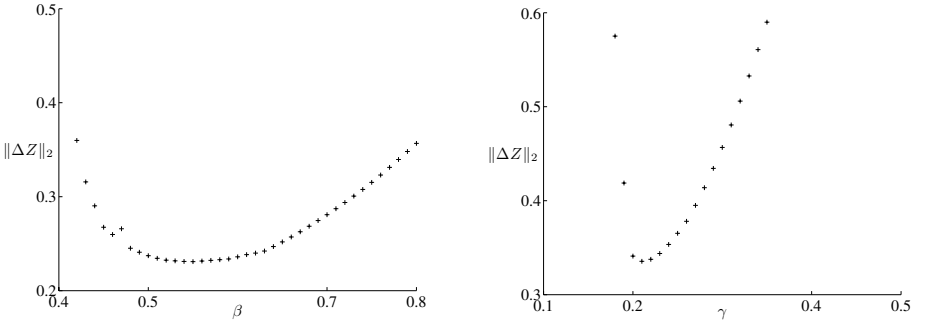


**Fig. 5.** Left: $\|\Delta Z\|_2$ in function of $\beta$, after $100 \times 128$ iterations of $IS_{\phi_1}$. Right: $\|\Delta Z\|_2$ in function of $\gamma$, after $100 \times 128$ iterations of $IS_{\phi_2}$. In these tests, the initialization $Z^0 = Z_{L_2}$ is used.

of the limit. Since similar curves are obtained for both other schemes, we decide to fix the number of iterations at $100 \times 128$ for all the tests. Of course, better stopping criteria could have been used, but this was not our main concern. Moreover, this first scheme is quite slow, due to the complexity of the formula (18) and (19): the CPU time of $100 \times 128$ iterations is equal to $17s$ on a P4 2.4 GHz, for a domain of reconstruction $\Omega$ which contains $128 \times 128$ points (the CPU times of both other new schemes is approximately the same). The resort to classical acceleration techniques, as for instance multi-grid methods, would probably be welcome.

The accuracy $\|\Delta Z\|_2$ of the 3D-reconstruction which is obtained after $100 \times 128$ iterations of the schemes $IS_{\phi_1}$, in function of $\beta$, is plotted on the left of Fig. 5. The best reconstruction, which is represented in Fig. 6, corresponds to $\|\Delta Z\|_2 = 0.23$ and is reached when $\beta = 0.55$ and $Z^0 = Z_{L_2}$ (see Fig. 2-right). It is qualitatively and quantitatively much better than the previous ones.

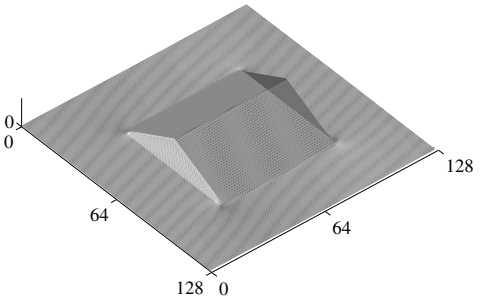


**Fig. 6.** 3D-reconstruction obtained using $IS_{\phi_1}$, for the optimal value $\beta^* = 0.55$ and $Z^0 = Z_{L_2}$: $\|\Delta Z\|_2 = 0.23$

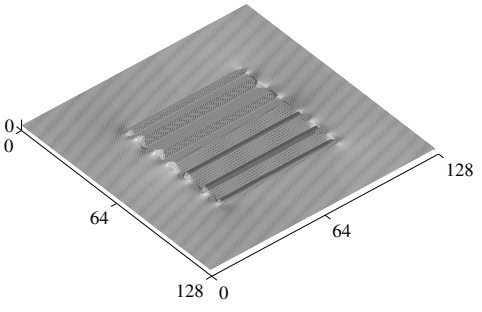


**Fig. 7.** 3D-reconstruction obtained using $IS_{\phi_1}$, for the optimal value $\beta^* = 0.55$ and $Z^0 = 0$: $\|\Delta Z\|_2 = 4.02$

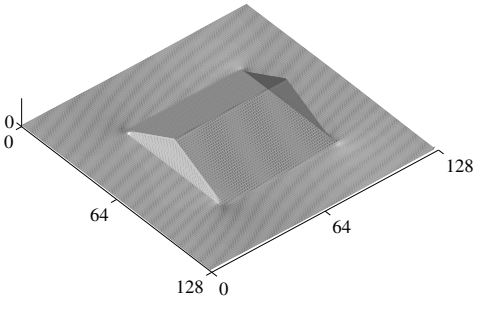


**Fig. 8.** 3D-reconstruction obtained using $IS_{\phi_2}$, for the optimal value $\gamma^* = 0.21$ and $Z^0 = Z_{L_2}$: $\|\Delta Z\|_2 = 0.36$

An important feature of the scheme $IS_{\phi_1}$ is its high sensitivity to the initial configuration $Z^0$. A second reconstruction, which is obtained with the same value of $\beta$ but $Z^0 = 0$, is represented in Fig. 7. It illustrates the existence of local minima for $\mathcal{F}_{\phi_1}(Z)$, as claimed in Section 4.3.

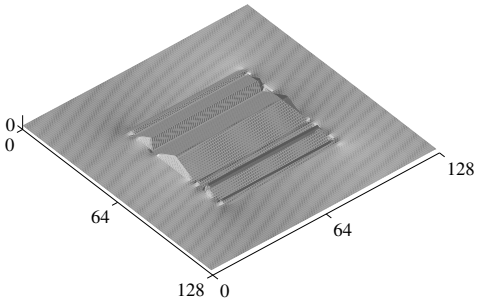


**Fig. 9.** 3D-reconstruction obtained using $IS_{\phi_2}$, for the optimal value $\gamma^* = 0.21$ and $Z^0 = 0$: $\|\Delta Z\|_2 = 3.39$

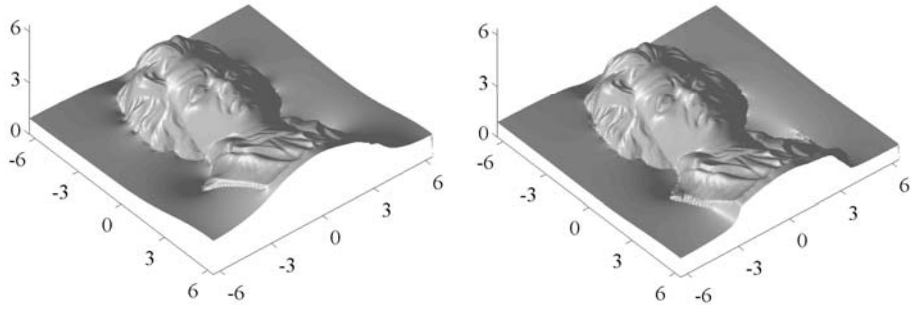


**Fig. 10.** 3D-reconstructions from the three photographs of the Beethoven's bustle, integrating the normal field using $IS_{L_2}$ (left) and $IS_{L_1}$ with $\alpha = 0.1$ (right) on $[1, 256] \times [1, 256]$

Finally, the accuracy $\|\Delta Z\|_2$ of the 3D-reconstruction which is obtained after $100 \times 128$ iterations of the scheme $IS_{\phi_2}$, in function of $\gamma$, is plotted on the right of Fig. 5. The best reconstruction, which is represented in Fig. 8, corresponds to $\|\Delta Z\|_2 = 0.36$ and is reached when $\gamma = 0.21$ and $Z^0 = Z_{L_2}$. It is approximately as satisfactory as the previous one. Nevertheless, a qualitative comparison between both curves in Figs. 5-left and 5-right tells us that $IS_{\phi_2}$ is more sensitive to $\gamma$ than $IS_{\phi_1}$ to $\beta$. A second reconstruction, which is a local minimum of $\mathcal{F}_{\phi_2}(Z)$, is represented in Fig. 9.

### 4.5 Application to Photometric Stereo

The part of the Beethoven's bustle which is visible in the photograph of Fig. 1-left does not contain self-occlusion. On the other hand, there is a discontinuity between the silhouette of the bustle and the background. Unfortunately, the background looks black in all these images, so that photometric stereo cannot be used at such pixels. In order to test the schemes $IS_{L_1}$, $IS_{\phi_1}$ and $IS_{\phi_2}$ on real data,

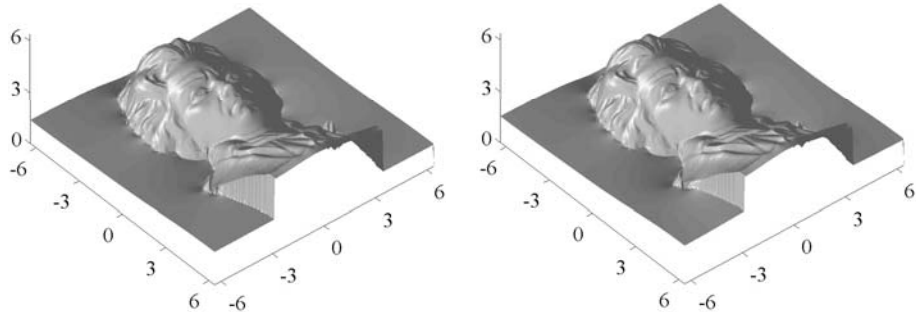


**Fig. 11.** 3D-reconstructions from the three photographs of the Beethoven's bustle, integrating the normal field using $IS_{\phi_1}$ with $\beta = 2$ (left) and $IS_{\phi_2}$ with $\gamma = 1$ (right) on $[1, 256] \times [1, 256]$

we consider the background as a plane with uniform normal $\mathbf{n} = [0, 0, 1]^t$. The reconstruction on the left of Fig. 10 is obtained using $IS_{L_2}$ on the whole domain $[1, 256] \times [1, 256]$, without prior segmentation. Obviously, the discontinuity is not well handled. On the other hand, the three reconstructions on the right of Fig. 10 and in Fig. 11 are obtained using $IS_{L_1}$, $IS_{\phi_1}$ and $IS_{\phi_2}$. The big gaps along the silhouette are rather well reconstructed, without any prior segmentation, as this was the case for the reconstruction of Fig. 1-right.

## 5 Conclusion and Perspectives

In this paper, after a theoretical study, we improve an existing method of normal integration. We show how to avoid prior segmentation, and consequently how to deal with possible discontinuities along silhouettes. More specifically, we prove the efficiency of non-convex regularization using $\phi$-functions. As an application, we successfully use two new methods of integration in the framework of photometric stereo. A first perspective of this work is to avoid the empirical estimation of the optimal value of the parameters, since all of the proposed methods of integration are parametric. Another perspective is to test other $\phi$-functions. As third perspective, we must question the way how the proposed methods face noisy normal fields (as this is done in [16]).

A last, but not least, perspective is to deal with multiview photometric stereo techniques, in order to produce complete 3D-reconstructions, and not only 2.5D-reconstructions (as, for instance, the surfaces shown in Figs. 1-right, 10 or 11). In [17], an interesting method of integration of a multiview normal field using a level set method is proposed, but the use of quadratic regularization makes it clearly impossible to retrieve the fine details of the 3D-shapes. In that work, as in [18], the silhouettes of the objects have to be segmented. Our new methods of integration could help avoiding this prior processing.

## References


1. Horn, B.K.P., Brooks, M.J.: The Variational Approach to Shape From Shading. Comp. Vis., Grap., and Im. Proc. 33(2), 174–208 (1986)
2. Wu, Z., Li, L.: A Line-Integration Based Method for Depth Recovery from Surface Normals. Comp. Vis., Grap., and Im. Proc. 43(1), 53–66 (1988)
3. Frankot, R.T., Chellappa, R.: A Method for Enforcing Integrability in Shape from Shading Algorithms. IEEE Trans. Patt. Anal. Mach. Intell. 10(4), 439–451 (1988)
4. Wei, T., Klette, R.: Depth Recovery from Noisy Gradient Vector Fields Using Regularization. In: Petkov, N., Westenberg, M.A. (eds.) CAIP 2003. LNCS, vol. 2756, pp. 116–123. Springer, Heidelberg (2003)
5. Durou, J.D., Courteille, F.: Integration of a Normal Field without Boundary Condition. In: Proc. 11th IEEE Int. Conf. Comp. Vis., 1st Workshop on Photometric Analysis for Computer Vision, Riode Janeiro, Brazil (October 2007)
6. Klette, R., Schlüns, K.: Height data from gradient fields. In: Proc. Machine Vision Applications, Architectures, and Systems Integration, Proceedings of the International Society for Optical Engineering, Boston, Massachusetts, USA, November 1996, vol. 2908, pp. 204–215 (1996)
7. Schlüns, K., Klette, R.: Local and global integration of discrete vector fields. In: Solina, F., Kropatsch, W.G., Klette, R., Bajcsy, R. (eds.) Advances in Computer Vision. Advances in Computing Science, pp. 149–158. Springer, Heidelberg (1997)
8. Horowitz, I., Kiryati, N.: Depth from Gradient Fields and Control Points: Bias Correction in Photometric Stereo. Im. and Vis. Comp. 22(9), 681–694 (2004)
9. Lempitsky, V., Boykov, Y.: Global Optimization for Shape Fitting. In: Proc. IEEE Conf. Comp. Vis. and Patt. Recog., Workshop on Beyond Multiview Geometry: Robust Estimation and Organization of Shapes from Multiple Cues, Minneapolis, Minnesota, USA (June 2007)
10. Simchony, T., Chellappa, R., Shao, M.: Direct Analytical Methods for Solving Poisson Equations in Computer Vision Problems. IEEE Trans. Patt. Anal. Mach. Intell. 12(5), 435–446 (1990)
11. Tankus, A., Kiryati, N.: Photometric Stereo under Perspective Projection. In: Proc. 10th IEEE Int. Conf. Comp. Vis., Beijing, China, October 2005, vol. I, pp. 611–616 (2005)
12. Basri, R., Jacobs, D.W., Kemelmacher, I.: Photometric Stereo with General, Unknown Lighting. Int. J. Comp. Vis. 72(3), 239–257 (2007)
13. Aubert, G., Kornprobst, P.: Mathematical Problems in Image Processing. Applied Mathematical Sciences, vol. 147. Springer, Heidelberg (2002)
14. Charbonnier, P., Blanc-Féraud, L., Aubert, G., Barlaud, M.: Deterministic edge-preserving regularization in computed imaging. IEEE Trans. Im. Proc. 6(2), 298–311 (1997)
15. Aujol, J.F., Durou, J.D.: Realistic integration of a dense normal field (submitted, 2009)
16. Fraile, R., Hancock, E.R.: Combinatorial Surface Integration. In: Proc. 18th Int. Conf. Patt. Recog., Hong Kong, August 2006, vol. I, pp. 59–62 (2006)
17. Chang, J.Y., Lee, K.M., Lee, S.U.: Multiview Normal Field Integration Using Level Set Methods. In: Proc. IEEE Conf. Comp. Vis. and Patt. Recog., Workshop on Beyond Multiview Geometry: Robust Estimation and Organization of Shapes from Multiple Cues, Minneapolis, Minnesota, USA (June 2007)
18. Hernández, C., Vogiatzis, G., Brostow, G.J., Stenger, B., Cipolla, R.: Multiview Photometric Stereo. IEEE Trans. Patt. Anal. Mach. Intell. 30(3), 548–554 (2008)